ACS OMEGA

Open Access

http://pubs.acs.org/journal/acsodf

Article

Material Characterization Study of Magnetite Nanocrystals for RF Sensing

Michael D. Sherburne,* Timothy A. Dreier, Benjamin H. Klitsner, Dale L. Huber, Sergei A. Ivanov, Chris Parks, Matt T. Simons, and Edl Schamiloglu

Cite This: *ACS Omega* 2024, 9, 41433−41445

Read Online

ACCESS | Metrics & More | Article Recommendations | Supporting Information

ABSTRACT: Magnetite nanocrystals show promise for electrically small gigahertz frequency applications, which could lead to miniaturizing transformer cores and new sensing technologies. This work presents a rigorous radiofrequency characterization of these nanocrystals using vector network analyzer (VNA) ferromagnetic resonance (FMR) measurements. For the first time, two different average diameters of Fe_3O_4 nanocrystals are investigated (7.3 and 20.2 nm). When the VNA−FMR results were compared to micromagnetic simulations, the magnetic anisotropy (K_1) deviated from the ideal mean orientation value of $K_1/2$ to $K_1/80$ for the 7.3 nm nanocrystal. In contrast, the obtained magnetic anisotropy in 20.2 nm nanocrystals slightly deviated to $K_1/11$ due to less structural deformations. These findings resulted in a newly proposed methodology for an approximate simulation based on VNA−FMR measurements. In addition, this work estimates the approximate amount of nanocrystals needed to measure a useful VNA−FMR spectrum.

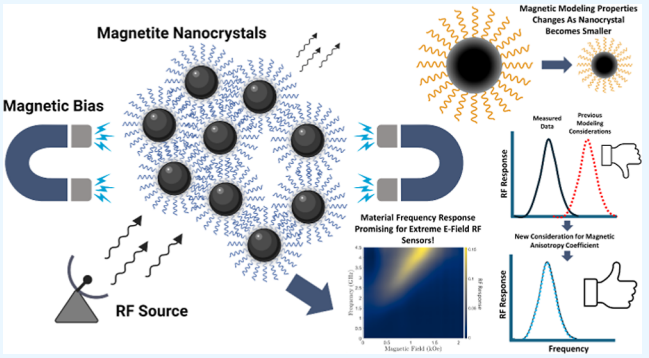

1. INTRODUCTION

Radio-frequency (RF) field sensors have a wide range of possible uses in measuring RF fields with applications ranging from pulsed power,[1] telecommunications,[2] and the automotive industry,[3] among others. When it comes to small spaces, measuring RF fields becomes more challenging. Conventional metal antennas can induce RF scattering and thus perturb the RF field that one wants to measure. This is where electro-optic (EO) sensors can play an important role. EO sensors for RF reception (EO/RF) are becoming more affordable, reliable, and accurate. Their relatively small size and small amount of conductive material compared to metal antennas make them ideal for RF measurements.[4−8] EO/RF usually contains, at most, an electrically small dipole antenna. The length of antenna is less than $\lambda/10$, where λ is the wavelength of the highest frequency of interest.[9−11] However, commercially available EO/RF is still about several centimeters in size. Fortunately, there is a way to make these EO/RF smaller by using nanoparticles (NPs). Recently, researchers have been looking at integrating EO materials with photonic crystal fibers (PCF)s.[12,13] To our knowledge, no one has investigated using nanomaterials drawn through PCFs for the purpose of RF sensing.[14−18] Instead of installing EO crystals onto the tips of these PCFs,[12] one could draw magnetically sensitive materials through the capillaries of these PCFs. Then, these PCFs can be paired with other nanomaterials such as quantum dots (QDs) or nanoplatelets (NPLs) to measure the incident RF by using changes in either the photoluminescence (PL) lifetime or the emission wavelength. A commonly used magnetically sensitive nanomaterial is magnetite (Fe_3O_4), which is superparamagnetic (SPM) at nanosize. The SPM property causes magnetite to respond to frequencies through the gigahertz range and heat up when irradiated with RF magnetic fields (H-field). This temperature increase can be beneficial for measuring the power density of an incident RF field. To tie this back to the use of QDs in PCFs for sensing RF fields, the heat produced by the magnetite nanocrystals under RF irradiation can then travel to nearby QDs. This in turn will change the temperature of the QDs, which causes their PL emission wavelength to change. One can then create a calibration setup to make an antenna factor curve that ties the power of the incident RF field to the amount of wavelength shift of the optical PL emission of the QDs. If additional circuitry can be used to add modulation, it would be possible to extract the frequency information from these materials.[19] The use of nanocrystals over magnetite micropowder is preferred as the specific loss power (the amount of heat generated through a changing magnetic field)

Received: May 14, 2024
Revised: September 18, 2024
Accepted: September 19, 2024
Published: September 24, 2024

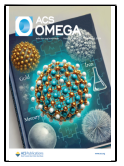

is 2 to 3 orders of magnitude larger than conventional methods of magnetic heating. These conventional methods consist of hysteresis and Néel and Brownian relaxation mechanisms, which produce lower amounts of thermal energy compared to resonant spin-excitation heating that occurs in magnetite nanocrystals.[20]

However, before the integration of magnetite NPs into PCFs or any other type of sensing system, the RF response needs to be characterized. One method is vector network analyzer ferromagnetic resonance (VNA−FMR) measurement.[20,21] A magnetite film is dropcast onto a microstrip line, and direct current (DC) H-field is orthogonally (axially) applied to the direction of the current flow (longitudinally) along the microstrip line to change the precessional frequency of the material's magnetization. The current flow along the microstrip line is established by sourcing power from port one of the VNA and returning the current into port two of the VNA. The ratio in power is the complex ratio of the input wave on port one to the output wave on port two.[22] This transmission coefficient (S_{21}) is important because changes in this coefficient in a VNA−FMR measurement can quantify the power being modified by the magnetite's RF response. The S_{21} is measured at both a large H_{DC} field (for comparative purposes) and at the H_{DC} field of interest. The difference between these two S_{21} measurements is known as ΔS_{21}. Then, one can use the ΔS_{21} spectra to empirically calculate the material coefficients: damping coefficient (α) and internal magnetization component of the applied magnetic field (H_{int}), which can be used for simulations.[20] Since these NPs have a random orientation of their magnetic moments as an ensemble of particles (essentially isotropic when it comes to magnetic measurements), one could then use these data for the design of a free-field or surface sensor. Previous papers have not provided information in regard to magnetite NPs across multiple diameters and applied amounts onto a microstrip line.[20,21,23−25] In addition, essential characteristics of the experimental setups such as the uniformity of the H-field and the uncertainty of the RF setup were not addressed either. This work significantly builds upon the previous papers for modeling of magnetite NPs to experimental data and provides additional RF characterizations of the apparatus and a look into how various amounts and diameters of magnetite NPs change the ΔS_{21} spectrum.

In this paper, we first present a theoretical justification behind this work, followed by the computational and experimental methodology, then the measured results, overall discussion, and the conclusion.

2. THEORY

This paper builds upon previous modeling and simulation work.[26] As the size of a magnetic particle decreases, it traverses the critical point where the material changes from a multidomain structure to having all its dipoles pointing in the same direction within a single domain. However, in general, it still is not considered an SPM state unless enough thermal energy is supplied to allow the individual single domain particles to reorient their moments. As such, the material becomes SPM below a threshold radius (the magnetic particle is considered spherical) when the present thermal energy is greater than the activation energy needed to allow the particle moment to freely reorient. In contrast to SPM particles, a magnetic particle could be micrometers in diameter and contain multiple magnetic domains and therefore be a multi domain magnetic particle. The activated reorientation allows an ensemble of particles to randomize their moments and therefore lead to the demagnetization of the ensemble (no coercivity) as illustrated in Figure 1. Coercivity is how strong a

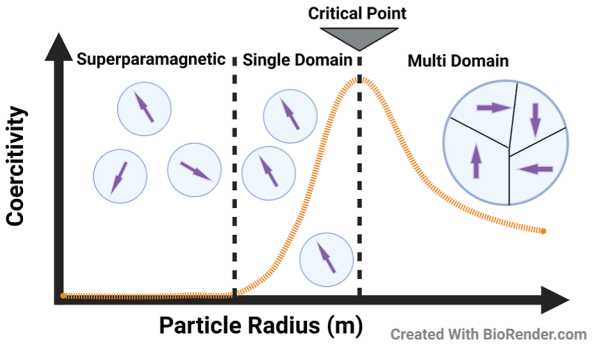

Figure 1. Illustration showing the different magnetic domain stages that a shrinking ferrous particle goes through until it ultimately becomes SPM.[30,31]

magnetic field needs to be in order to make a magnetic material go from saturation (e.g., all magnetic dipoles are aligned and cannot be aligned anymore) back to zero (e.g., magnetic dipoles are randomly oriented). In addition, the higher the coercivity, the more energy that needs to be exerted in order to rotate the magnetic dipoles within a material. Materials with a high coercivity are usually used as permanent magnets.[27−29]

Typical heating mechanisms such as Néel and Brownian relaxations are not fast enough to generate heat at gigahertz frequencies.[32] Even with small, SPM magnetite NPs (≤20 nm), hysteresis heating plays a minimal role at these frequencies. For gigahertz frequencies, a mechanism called resonant spin-excitation and dissipation comes into play and becomes the predominant heating mechanism.[20] At the right excitation frequency, the magnetic moment can precess around the direction of the applied direct current magnetic field. As it is dampened, it releases precessional energy as heat. The Landau−Lifshitz−Gilbert (LLG) equation explains this resonant response and in a modified form is given as

$$\frac{\partial \mathbf{M}}{\partial t} = -\gamma \mathbf{M} \times \mathbf{H}_{eff} + \frac{\alpha}{M_s}\mathbf{M} \times \frac{\partial \mathbf{M}}{\partial t} \quad (1)$$

where γ is the gyromagnetic ratio, α is the damping coefficient, $\mathbf{H}_{eff}$ is the applied H-field (including the components of the RF magnetic field and the internal magnetic field), M_s is the magnetization saturation, and $\mathbf{M}$ is the magnetization of the material.[26] The heating from this mechanism is anywhere from 2 to 3 orders of magnitude larger than is observed with conventional induction heating.[20] First-principles and numerical finite-difference-time-domain (FDTD) modeling results are provided in the ref 26. In order to use these models, one must know the α and H_{int} (internal magnetization component of $\mathbf{H}_{eff}$), which have to be derived from empirical data. In addition, the saturation magnetization M_s of the magnetic NPs must be determined. This paper uses material characterization data from collected measurements (determined in this manuscript) and LLG parameters from previous works[20,26] to make approximate predictions in regards to the RF precessional response of magnetite NPs.

https://doi.org/10.1021/acsomega.4c04589
ACS Omega 2024, 9, 41433−41445

3. METHODOLOGY

Magnetite NPs were made using the process presented in Vreeland et al.[33] Two batches of Fe_3O_4 NPs with two different average diameters were synthesized for this work: 20.2 and 7.3 nm. The size distributions were determined by using small-angle X-ray scattering (SAXS) of particle solutions in hexane filtered through a 0.22 μm filter. From the best-fit curves for the SAXS data, the particle size distribution was determined to be 5.7% for the 20.2 nm NPs and 13.5% for the 7.3 nm NPs. The SAXS data is presented in Figure S1 of Supporting Information. Transmission electron microscopy (TEM) images were acquired with a Technai TEM Q30 at a gun voltage of 300 keV for each specimen on copper grids and can be seen in Figure 2.

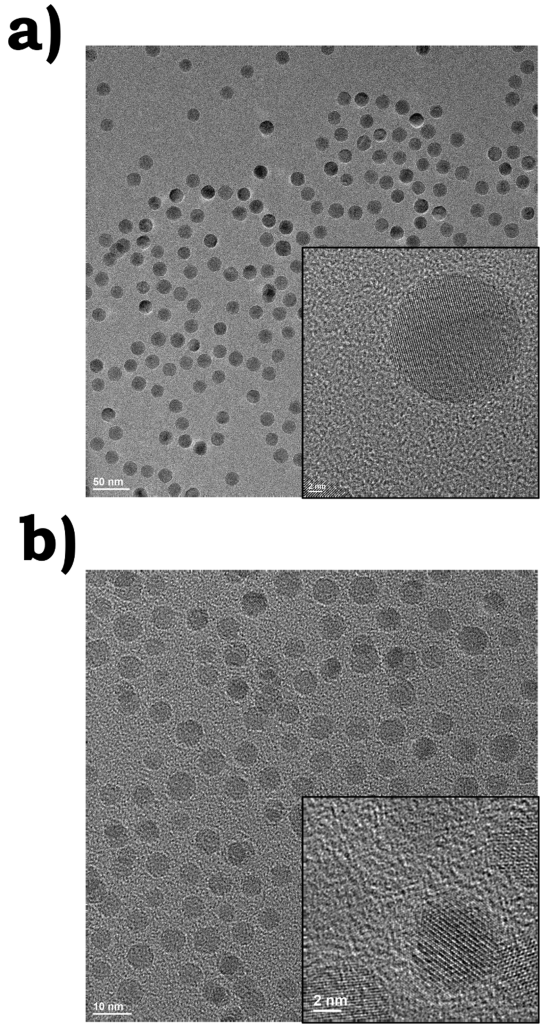

Figure 2. (a,b) TEM images for 20.2 and 7.3 nm average diameter NP specimens, respectively.

The Fe_3O_4 phase of synthesized NPs was confirmed with X-ray diffraction (XRD) (SmartLab II Rigaku, Cu Kα radiation, in Parallel beam geometry), and the corresponding diffraction pattern can be seen in S15. Finally, the $M-H$ curves were obtained with Quantum Designs Versalab Vibrating Sample Magnetometer (VSM) for both 20.2 and 7.3 nm NPs and are presented in Figure 3.

Presented data in Figure 3 reveal that both batches of NPs were SPM (negligible area within the hysteresis curve). The saturation magnetization (M_s) values for 20.2 and 7.3 nm NPs were 76.3 and 8.7 emu/g, respectively. The zero field cooling measurements for both diameters are presented in Figure S11. Before applying the magnetite materials to microstrip boards, the concentration of NPs in each sample was determined by weighing the amount of pure Fe_3O_4 after the removal of a known amount of solvent and removal of all ligands from the particles upon heating the sample to 400 °C in an inert atmosphere in a thermogravimetric analysis experiment. For the magnetite stock used in this article, 20.2 and 7.3 nm had a concentration of 3.11 and 15.00 mg/mL, respectively.

The 20.2 nm NPs were applied to three copies of a microstrip PCB in varying amounts. These copies were labeled B1, B2, and B3. They had 1.00 0.50, and 0.25 mL of solution deposited on the boards, respectively. Before deposition, the amounts were further concentrated by evaporation, until the solution became viscous. This viscous solution was dropcast onto a microstrip. The resulting amounts of magnetite NPs applied to the B1, B2, and B3 microstrips were 2.59, 1.85, and 0.64 mg, respectively. Smaller NPs were deposited in a manner similar to that for 20.2 nm NPs to the boards labeled B4, B5, and B6. First, the 7.3 nm magnetite solution was diluted until its concentration was 3.92 mg/mL. The amount dropcast was then 0.80, 0.40, and 0.20 mL, respectively. The resulting amounts of deposited NPs onto B4, B5, and B6 microstrips were 4.77, 2.48, and 0.79 mg, respectively. From appearance, the dropcast 4.77 and 2.48 mg should not be possible due what would be more mass than could be dropped onto the line. However, the solution being more concentrated than the 20.2 nm solution could increase the likelihood of agglomeration. This can lead to dropcasting more material than intended and an additional check being done to measure the true amount of material deposited. Additional details of the microstrip design and performance can be found in the Supporting Information section. Furthermore, photographs of the deposited magnetite films can be seen in Figure S6. The reason we used a microstrip architecture as opposed to the coplanar waveguide was due to both cost and measuring frequencies up to the C-band to make a measurable FMR trend. The losses were tolerable for the VNA being used (S_{21} of −0.76 dB at 4.5 GHz) and did not affect the uncertainty of the measurement. This approach allowed for the preparation of an affordable PCB, which, in turn, allowed for the testing of several NP magnetite film factors (amount of applied NPs and NP diameters) at no loss of measurement performance.

The VNA−FMR experimental setup started with the CW RF signal emitting from port one of an 18 GHz VNA (model: Agilent Technologies E5063A). The VNA was used with the following settings: starting frequency (10 MHz), ending frequency (4.5 GHz), number of linearly equidistant frequency steps (201), intermediate frequency (IF) bandwidth filter (10 Hz), no averaging used, and power output set to 0 dBm. The VNA measurements were conducted at thermal equilibrium by leaving it on for 1 h. A short-open-through-load (SOLT) two-port calibration was performed up to the male SubMiniature version A (SMA) jacks on the microstrip line PCB using a Maury 8050CK calibration kit. The VNA signal travels from port one through a DC block (model: Mini-Circuits GP-18+), through the RF cable (model: RG-142), and then through two nonmagnetic RF connectors (model: Cinch 142-0901-821 and model: Amphenol RF ACX1240-ND). The other part of the RF signal travels through the nonmagnetic SMA jack (model: Würth Elektronik 60311002114501) into the microstrip line

https://doi.org/10.1021/acsomega.4c04589
ACS Omega 2024, 9, 41433−41445

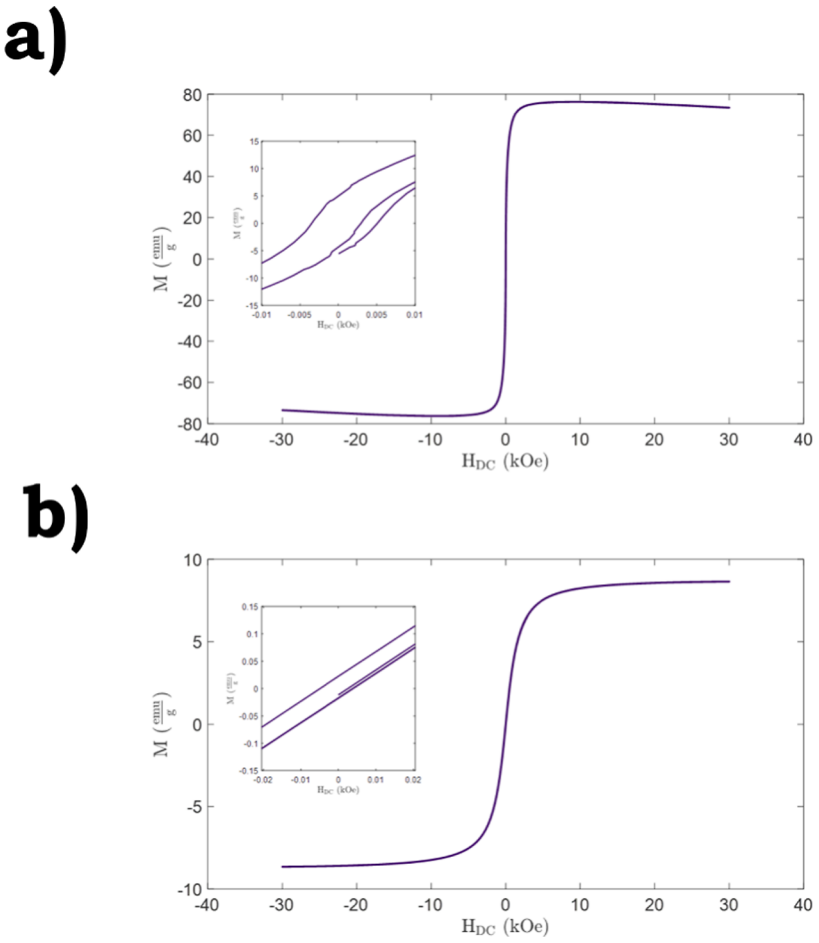

Figure 3. Magnetic hysteresis curves for both the (a) 20.2 nm NPs and (b) 7.3 nm NPs.

and out of the other end of the microstrip. The signal travels through the same circuitry as mentioned above into port two of the VNA. The setup illustration can be seen in Figure 4.

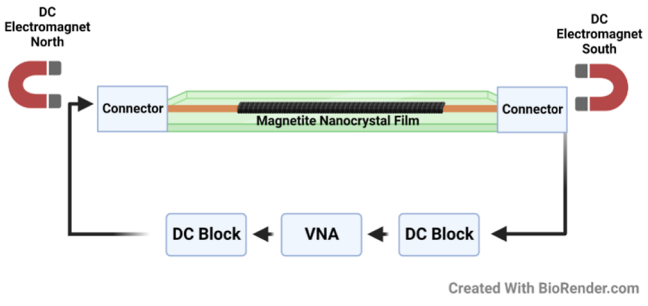

Figure 4. Setup of VNA−FMR measurement used for this experiment. Port one of the VNA goes through a DC block, then into a microstrip line loaded with magnetite NPs, and then back through another DC block and into port two of the VNA.

DC magnetic field strengths were swept between 18.0 and 2.103 kOe at ≈16.0 Oe steps (measured at the center of the microstrip line) using a water-cooled DC electromagnet (model: GMW MagnetSystems model 3470). This electromagnet was attached to a water chiller model: (Fisher Scientific Isotemp model 900). Cooling plate temperatures were kept to be in between 17 and 20 °C. The temperature was monitored using a temperature fiber optic sensor (model: Biopac Systems Inc. TSD181) attached to an electromagnet cooling plate on the liquid cooling outlet side with a fiber optic sensor controller (model: Biopac Systems Inc. FOTS100). The magnetic field strength was measured by using a Gauss meter (model: TD8620). The Gauss meter's readings were zeroed at background before taking measurements between the yokes of the electromagnet. A wooden jig and plastic screws were used to secure the microstrip PCBs between the yokes of the electromagnet. For calculating the ΔS_{21} spectrum, the reference S_{21} spectrum is taken at a H_{DC} field of 3.5 kOe and subtracted from the S_{21} spectrum with an applied H_{DC} field of lower magnetic field strength.[20] Note, it is not important to know the true rms power going into the microstrip due to VNA−FMR being a relative measurement, as long as the rms power does not substantially change the magnetization or material coefficients of the NPs. In addition, measuring the S_{21} or the S_{12} (reversed current direction along the microstrip) does not matter since the H_{AC} field generated by the microstrip line was orthogonal to the applied H_{DC} field and the NP ensemble would demonstrate the same magnetic response whether the current was flowing toward one end of the applied H_{DC} field or the other. This theory was confirmed when comparing the two current directions, where their small differences may be described by the uncertainty of the measurement. Measurements for samples B1 and B4 were taken three times. The data were then plotted with the *x*-axis as the magnetic field bias and the *y*-axis as the frequency. A linear fit line was applied along the region where the magnetite NPs were sufficiently magnetically saturated. The slope of the linear

https://doi.org/10.1021/acsomega.4c04589
ACS Omega 2024, 9, 41433−41445

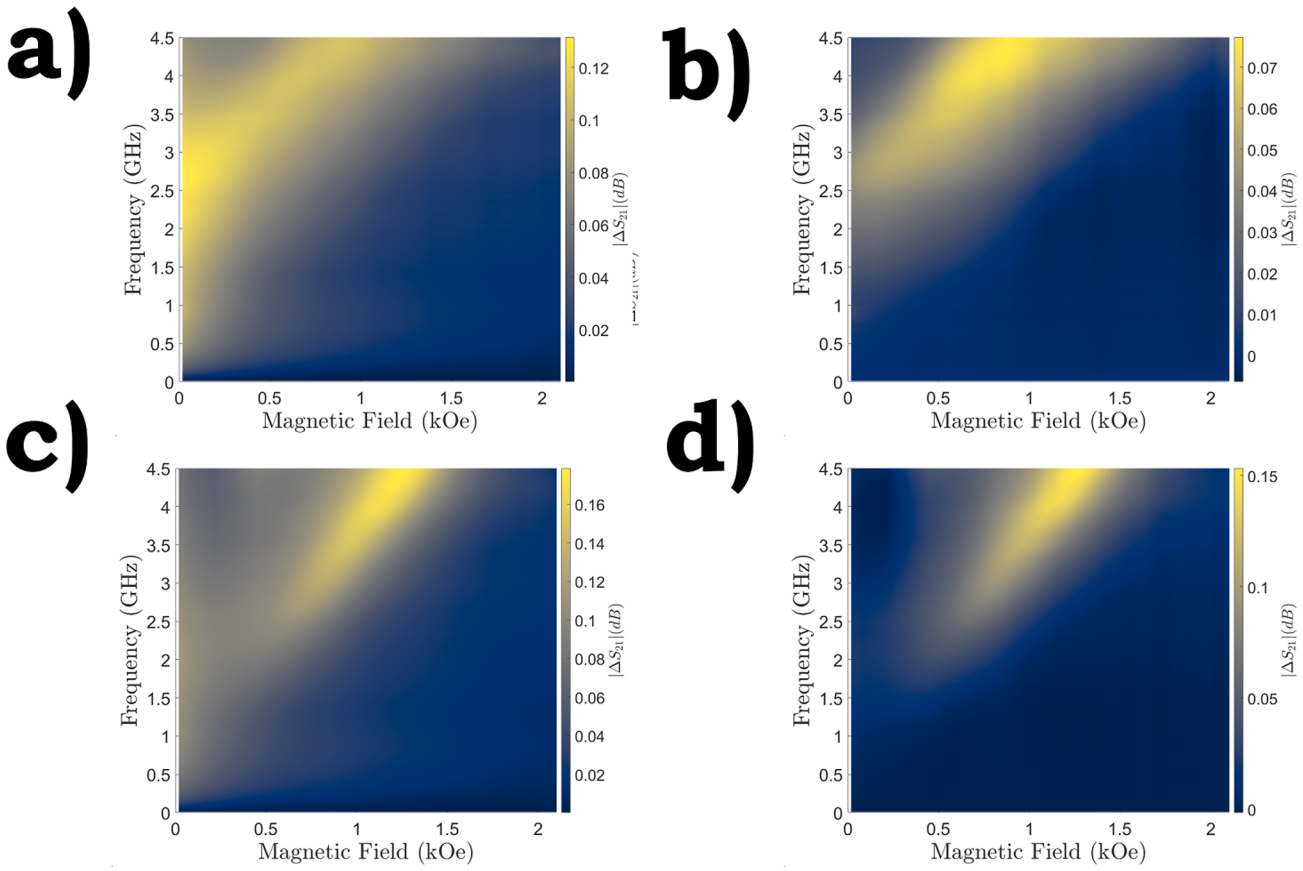

Figure 5. ΔS_{21} spectrum of (a) sample B1 without control subtracted out. (b) Sample B1 with control subtracted out. (c) Sample B4 without control subtracted out. (d) Sample B4 with control subtracted out. Notice large ΔS_{21} contribution when control is not subtracted out at low (<500 Oe) H_{DC} fields. All plots used 7.5% moving-average smoothing applied over both the frequency and magnetic field.

fit in MHz/Oe was used to get the γ_{0m} coefficient. From here, a ratio of the magnetite γ_0 (2.8 MHz/Oe) to the measured γ_{0m} was used to calculate the α coefficient using the relation $\alpha = \sqrt{\left|\frac{\gamma_0}{\gamma_{0m}} - 1\right|}$.[20] H_{int} was calculated by using the frequency point where the linear fit line intersects the y-axis (f_{inter}) and using the relation $H_{int} = \frac{f_{inter}(1+\alpha^2)}{\gamma_0}$.[20,34]

Micromagnetic simulations of the magnetite NPs were performed in Ubermag. The K_1 coefficient was 1.36×10^4 J/m^3, and the A_{ex} coefficient was 13.2×10^{-12} J/m. A mean orientation value for the K_1 coefficient was used to account for the random magnetic anisotropy directions by dividing K_1 by two.[20] The number of units cells used for both the 20.2 and 7.3 nm NPs were four and one cells, respectively. The simulation ran for 100 ns, and a sinc excitation function (center frequency of 10 GHz) was applied at 30 ns. 2000 linearly equidistant data points were used. The H_{AC} excitation was applied orthogonal to the H_{DC} field.[26]

4. RESULTS AND DISCUSSION

Six microstrips with two diameters of magnetite NPs with three different amounts of magnetite for each diameter were tested after being dropcast onto these strips. The labeling scheme for what each microstrip contained can be read in the methodology section. The VNA−FMR spectra for B1−B6 can be seen in Figure S9 of the Supporting Information. As the amount of NPs applied to the microstrip was reduced, the ability to accurately determine the resonance of the VNA−FMR spectra deteriorated. For our measurements, we found that when comparing the deposited mass of magnetite across each of the microstrip lines, the amount of material across the entire length of the transmission line (10.16 mm in our experiment) should not become lower than 0.5 μg (on average) across a 4.14 μm × 1.70 mm surface area in order to get informative VNA−FMR spectra. The data supporting this can be seen in Section 12 of the Supporting Information. This amount should be applied across the entire length of the microstrip. Small regions containing more than 0.5 μg (thicker films) that were present together with regions of less than 0.5 μg across the length of the strip line do not increase the ability to determine the resonance of the VNA−FMR spectra. We found that being able to approximately determine the resonance of the VNA−FMR spectra was dependent upon the overall length of the microstrip that contained ≈0.5 μg (on average) across a 4.14 μm × 1.70 mm surface area. After running an initial test of all microstrips (B1−B6), we determined that only B1 and B4 should be used to compare the effect of two different diameters of magnetite NPs due to being able to accurately see resonance in both samples (B1 and B4 being the largest amounts of magnetite NPs dropcast onto the microstrips for their respective diameters).

Initial results show large changes in ΔS_{21} across frequency at a given H_{DC} field (spectral broadening) for sample B1 with a small 18.1 Oe H_{DC} residual bias. The spectral broadening artifacts of the ΔS_{21} seen in both Figure 5a,c were removed by

https://doi.org/10.1021/acsomega.4c04589
ACS Omega 2024, 9, 41433−41445

subtracting out the control measurement of the microstrip (see control spectra in Figure S8).

Despite using printed circuit board (PCB) material that is considered nonferrous and assumingly nonmagnetic, large changes in the ΔS_{21} spectra were observed. This was most likely due to the magnetic material content within the RG-142 coaxial cable; the inner conductor was made of silver-coated copper-clad steel. As can be seen in Figure S8 of the nonloaded PCB control, ΔS_{21} decreases at higher frequencies. This shows that the skin effect plays a major role in the signal absorption loss. According to the equation for skin depth, the higher the frequency, the less the RF signal penetrates the coaxial wire.[35] Lower penetration into the coaxial cable causes the steel core to have less of an effect on the RF signal. In addition, ΔS_{21} became zero after a sufficiently large H_{DC} field was applied. This shows that the cable contains magnetic material and the magnetic domains within this material completely saturate where all the magnetic dipoles are pointing in the same direction (therefore, it cannot continue to absorb RF current in a traditional magnetic field hysteresis loop sense). There were magnetic impurities in other materials used in both the PCB and the solder (judging by their ferromagnetic response, Figure S13). However, the contribution of these impurities into the overall device magnetization was much smaller in comparison to that of steel inner conductors due to the removal of the control ΔS_{21} primarily affecting the low H_{DC} magnetization, whereas the higher H_{DC} magnetization showed minimal changes. For our measurements, we found that it is necessary to measure the control of one's transmission line setup. The use of higher quality nonmagnetic materials, including RF coaxial cables, might result in a reduction of broadening that would occur in a VNA−FMR spectrum.

As can be seen in Figure 6, there were two clear VNA−FMR trends between the 20.2 and 7.3 nm diameter NPs. A best-fit line can then be applied to the data along their linear regions.

First, the data collected with the 20.2 nm NP film had a lower slope along its main linear region compared to that of the 7.3 nm NP. The slope of the 20.2 nm NPs is 2.54 MHz/Oe and that of the 7.3 nm NPs is 2.60 MHz/Oe. The calculated slopes can be considered only estimates. Largely, this came from the uncertainty of the peak resonance along each H_{DC} data point. With uncertainty of the applied H_{DC}, the exact resonance frequency peak can be higher or lower at a given applied H_{DC} which could make the overall average best-fit line not produce material coefficient values that would allow for modeling to reproduce the ΔS_{21} spectrum. This can first be addressed by running a set of five different best-fit lines across the bounds of the resonance spectrum. Then selecting the line that produces material parameters accurately represented the ΔS_{21} in the magnetic saturated region where the ΔS_{21} is expected to correlate in a linear manner. This feedback process with simulation helps to eliminate making this process purely an arbitrary selection in the formation of a best-fit line. The lower bound is selected by picking points where the NPs are sufficiently magnetically saturated (VNA−FMR spectrum shows a single linear trend through higher frequencies). This is ≈230 Oe for the 20.2 nm NPs and ≈620 Oe for the 7.3 nm NPs. The upper bound is selected by picking points where the ΔS_{21} spectrum still has well-defined resonance peaks. This is ≈761 Oe for the 20.2 nm NPs and ≈1.216 kOe for the 7.3 nm NPs.

The preferred way to compare the simulated magnetic susceptibility to the measured ΔS_{21} is to reference Rosensweig's magnetic power dissipation equation, where the power dissipation is expressed as $P = \mu_0 \pi \chi'' f H_0^2$.[32] Note that Rosensweig's equation was originally designed for Néel and Brownian energy losses (inductive heating); however, the same concepts expressed within Rosensweig's work could be applied to precessional energy losses as well. The real part of the magnetic susceptibility χ' is not taken into account when looking at the power dissipation, because χ'' is the loss component. In our VNA−FMR experiment, we looked at the wave parameter ratio [the ratio between the transmitted wave (numerator) and the incident wave (denominator)] that the VNA was measuring from both its ports, and the ΔS_{21} corresponded to transmission power losses as the magnetite NPs experienced varying amounts of magnetic precessional energy losses. We can safely assume that any reflective (mismatch) loss of the transmission line is negligible due to keeping S_{11} less than −20 dB across the frequencies being

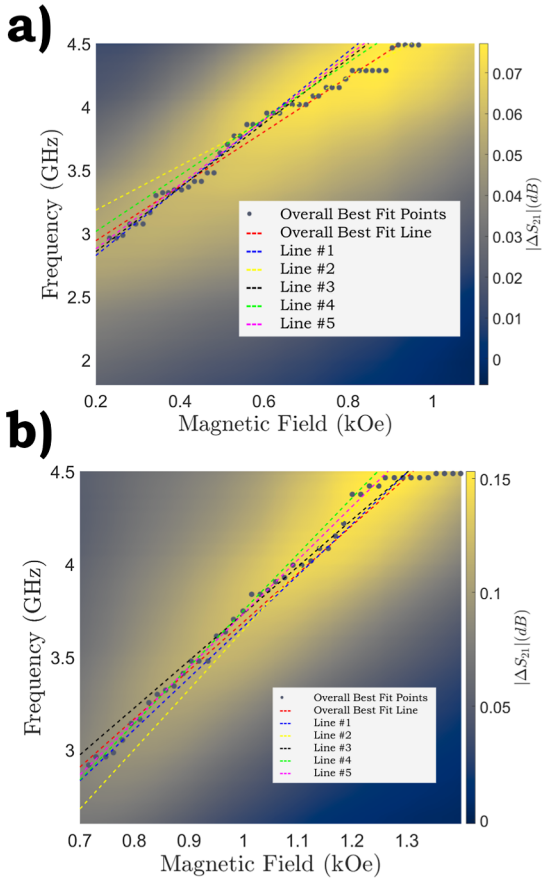

Figure 6. ΔS_{21} spectrum for both (a) 20.2 and (b) 7.3 nm average diameters. Overall best-fit lines going through the entire linear region along with the data points used (maximum ΔS_{21} for each H_{DC} field point) which correspond to the H_{DC} field ranges of 232.3−966.8 and 621.4−1399.0 Oe to create the best-fit lines are plotted for both (a,b). The additional five best-fit lines are taken along a window of data points along the H_{DC} field within the linear region for both (a,b). The H_{DC} field windows for (a) best-fit lines are 311.8−649.7 Oe for line #1, 494.9−761.4 Oe for line #2, 232.3−699.4 Oe for line #3, 494.9−649.7 Oe for line #4, and 264−699.4 Oe for line #5. The H_{DC} field windows for (b) best-fit lines are 699.4−1200.1 Oe for line #1, 1091.1−1200.1 Oe for line #2, 934.8−1155.8 Oe for line #3, 778.2−1015.1 Oe for line #4, and 621.4−1091.1 Oe for line #5. All plots used 7.5% moving-average smoothing applied over both the frequency and magnetic field. Color map from ref 36.

https://doi.org/10.1021/acsomega.4c04589
ACS Omega 2024, 9, 41433−41445

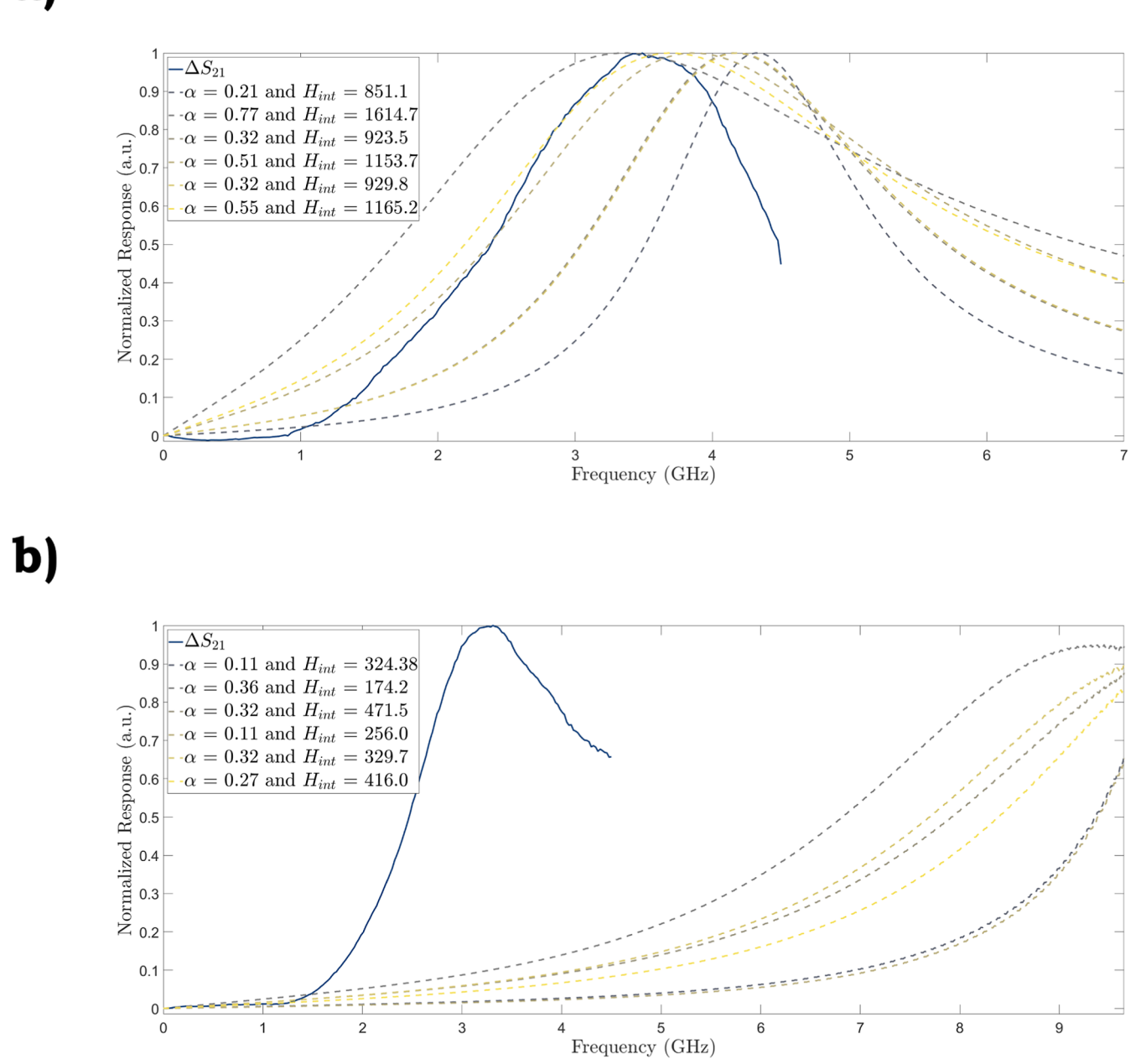

Figure 7. (a) 20.2 nm NP simulation done at a H_{DC} of 464.6 Oe and compared to ΔS_{21} data using five different best-fit lines. (b) 7.3 nm NP simulation done at a H_{DC} of 809.6 Oe and compared to ΔS_{21} data using five different best-fit lines.

measured as shown in S4 of the Supporting Information. Hence, we approximate that transmission coefficient changes correspond to the imaginary component of the magnetic susceptibility χ''.

Using the Ubermag micromagnetic code reported earlier,[26] the VNA−FMR spectral trends can be simulated from the magnetic susceptibility of a SPM material.[26] In order to ensure that the best-fit lines were ideal for the simulation, a spread of five different lines was made by choosing various points along the ΔS_{21} spectrum. The α and H_{int} values were then used in the simulations and plotted against a slice of the ΔS_{21} spectrum at a certain H_{DC} field. These H_{DC} slices were located at 464.6 and 809.6 Oe for 20.2 and 7.3 nm NPs, respectively. The simulation spreads for the five best-fit lines can be seen in Figure 7.

The simulated curves in Figure 7 were off from the ΔS_{21} peak; therefore, the closest peak FMR shapes were selected for each NP diameter. Next, the first order cubic magnetic anisotropy constant (K_1) value was adjusted from its bulk magnetite value (-1.36×10^4) J m^{-3} until the peak frequency location matched. The K_1 coefficient affects the H_{eff} term in the LLG equation and represents the magnetization angle-dependent change in magnetic energy. The coefficient value is determined by the symmetry of the crystal structure; hence, any crystal structure changes influence the value of K_1.[37,38] Two different H_{DC} slices were compared to assess whether the simulation can track the FMR peaks from the same material coefficient values. This resulted in the material coefficients for each NP diameter, as seen in Figure 8.

https://doi.org/10.1021/acsomega.4c04589
ACS Omega 2024, 9, 41433−41445

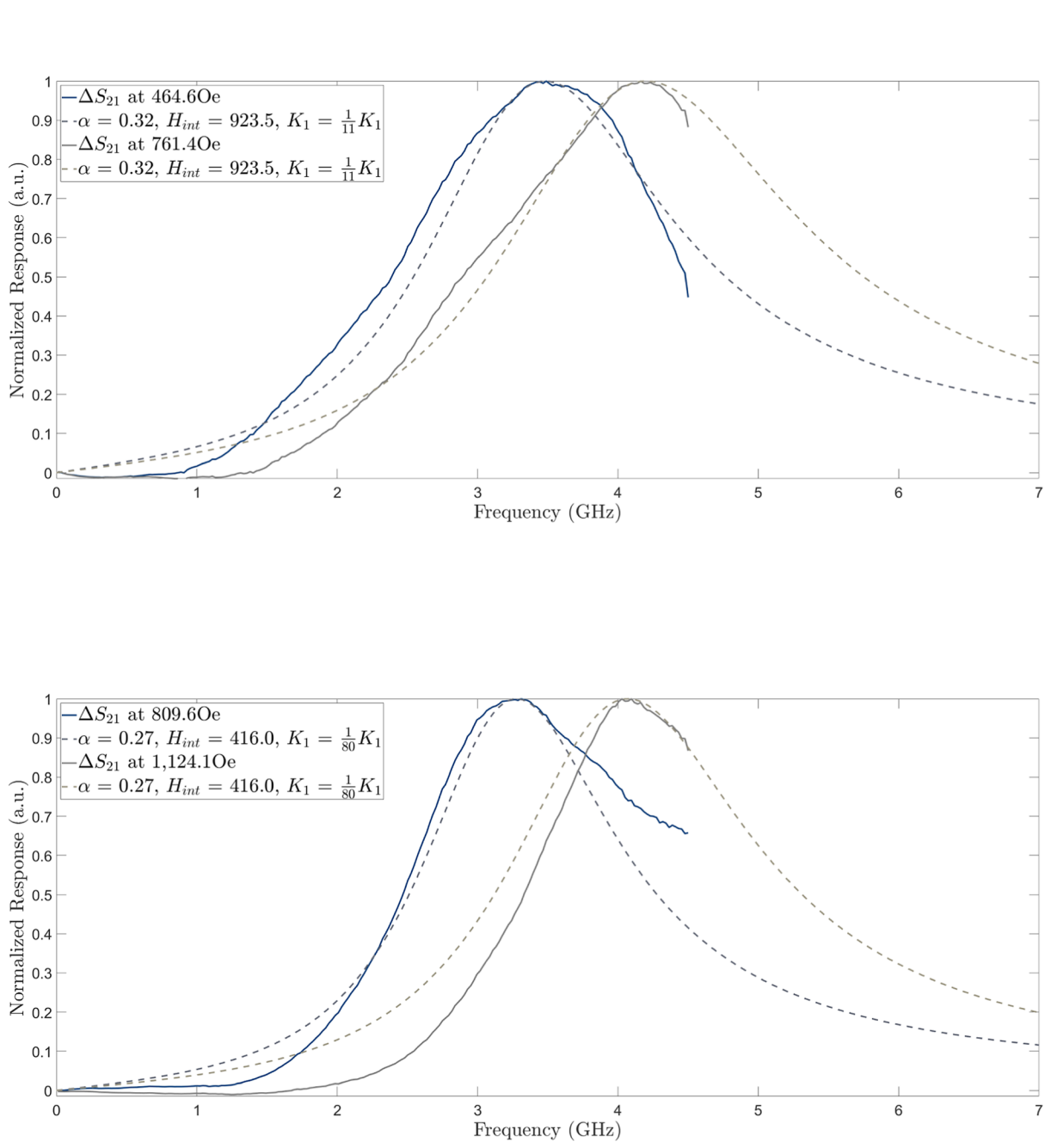

Figure 8. (a) 20.2 nm NP simulation compared to the ΔS_{21} at H_{DC} values of 464.6 and 761.4 Oe. (b) 7.3 nm NP simulation compared to the ΔS_{21} at H_{DC} values of 809.6 and 1124.1 Oe.

The magnetic material parameters of α and H_{int} for the 20.2 nm NPs were 0.32 and 923.5 Oe, respectively. For the 7.3 nm NPs, they were 0.27 and 416.0 Oe, respectively. The K_1 coefficients were adjusted to be $\frac{1}{11}K_1$ and $\frac{1}{80}K_1$ for the 20.2 and 7.3 nm NPs, respectively. Figure 8 shows that the simulated FMR curves were similar to the ΔS_{21} data but had some discrepancy. The discrepancy may be attributed to the particle size dispersion and the makeup of the film. The changes in the K_1 coefficient may also be due to variations in how the magnetite film dried. Alternatively, the discrepancy may be caused by the lattice spacing and NP structure deviations from bulk values, which might induce a preference for a specific magnetic field direction in 7.3 nm NPs compared with larger 20.2 nm NPs. All these factors may be responsible for the much larger change in the K_1 coefficient in the case of the 7.3 nm NPs than the change seen in the 20.2 nm NP when compared to the average random magnetic anisotropy direction coefficient value of $K_1/2$.[20] As smaller particles have higher surface energy, the interatomic distance on the surface changes between 7.3 nm NPs and the 20.2 nm NPs, which in turn, can influence the particle magnetic anisotropy.[39] Finally, the larger H_{int} value for the 20.2 nm NPs may also be partially attributed to interparticle interaction effects larger than those of the smaller 7.3 nm NPs.

The full width at half-maximum (fwhm) of the ΔS_{21} spectrum (how wide the spectrum spreads across frequency range at a given applied H_{DC} field) comes from a number of

https://doi.org/10.1021/acsomega.4c04589
ACS Omega 2024, 9, 41433−41445

effects. It appears that ΔS_{21} spectral broadening was not due to macroscale thermal changes, as explained in part S7 of the Supporting Information, but likely due to a spread of H_{DC} magnetic field strengths with a gradient across the microstrip and thermally induced changes of the electromagnet used in the experiment that influenced the H_{DC} fields. In addition, when adding the uncertainty associated with the 7.5% smoothing needed to reduce VNA artifacts (periodic oscillations across frequency due to ΔS_{21} being close to the 0.1 dB uncertainty of the VNA), the overall H_{DC} magnetic field strength uncertainty became 181 Oe 24 Oe from the change in the measured H_{DC} magnetic field at a given H_{DC} and 158 Oe from the 7.5% smoothing. Hence, the motivation is in applying five best-fit lines and seeing which one best matches with the VNA−FMR peak of the ΔS_{21} data. This is discussed further in Figure S10 of Supporting Information. In addition, the H_{AC} field changes across both the width and the length of the microstrip, as shown in both simulation (Figure S4) and measurement (Figure S5). However, unless the H_{AC} field is of sufficient magnitude to cause a significant thermal change of the magnetite nanocrystals, it will not influence the broadening of the ΔS_{21}. Furthermore, each NP ensemble has a nonzero size distribution, and these particles had varying levels of film thicknesses along the strip lines. In general, for a given magnetite particle diameter, the density of magnetite remains the same regardless of the film thickness due to the magnetite NPs being separated by their ligands. However, how the NPs dried may result in the formation of small voids (air pockets) within the film. These possible air pockets may cause changes in the magnetic interaction between surrounding NPs around these air pocket boundaries. The inhomogeneity in deposition may result in varying levels of interactions between particles, which can influence the size of the dispersion. For an initial assessment of a source of ΔS_{21} spectral broadening, the thickness profiles for each of the magnetite films were compared to the fwhm of the ΔS_{21} peaks (see Figure S12 for details). In general, a plausible trend emerges that connects the fwhm of the ΔS_{21} spectrum to the thickness of the film on top of the microstrip. This may possibly be due to the formation of small voids within the film, which would change the degree of magnetic interaction between neighboring NPs. This is a known property that the magnetic properties of SPM NPs can be significantly altered by magnetic interactions with neighboring NPs. This may also influence the spectral spread in the ΔS_{21} spectrum, e.g., see superspin glass discussion in refs 40−42. Finally, internal heating at the nanoscale may play a role in thicker films as well. This spectral broadening of the ΔS_{21} spectrum from the various aforementioned sources of ΔS_{21} effects may have created nonlinear variations that made the best-fit line approximation method difficult to apply.

It was important to confirm the measurement uncertainty after a rough estimate that considers those in the VNA's (≈0.1 dB at 4.5 GHz) and the two RF coaxial connections (0.1 dB per connection) at an IF bandwidth of 10 Hz (0.1 dB for the VNA used in this experiment using the SOLT two-port calibration from a Maury 8050CK calibration kit), which is calculated by the root sum of squares as $\sqrt{0.1^2 + 0.1^2 + 0.1^2}$ and results in an uncertainty of 0.173 dB. This uncertainty is comparable with the ΔS_{21} value for both magnetite samples. In addition, uncertainty is influenced at higher frequencies above 3.062 and 2.884 GHz for 20.2 nm loaded NPs and 7.3 nm loaded NPs while in the electromagnetic apparatus, respectively, due to the S_{11} going below −20 dB, which results in reflections starting to have a non-negligible small contribution to the measured data. The largest S_{11} measured was −14.1 dB (about 4%). Thus, without the use of more expensive equipment such as a RF lock-in amplifier to improve the signal-to-noise (SNR) ratio of the ΔS_{21}, uncertainty of gyromagnetic coefficient measurements using VNA−FMR becomes significant, and the importance of a direct comparison of the best-fit lines to simulation becomes imperative for reasonable gyromagnetic coefficient data. In addition, the S_{11} is influenced by (1) material loading and (2) tension of the RF connectors in the electromagnetic apparatus. Stiff RF cables are not ideal for this experiment, as they can create strain on the RF connectors and cables, which can thereby change the S_{11} at higher frequencies. The repeatability of the measurements is taken as the maximum difference between the three repetitions of the measurements in both the S_{21} and S_{12} current directions after subtracting their respective controls (transmission line is connected and disconnected between each sweep). The repeatabilities for the 20.2 and 7.3 nm VNA−FMR spectra were ±0.006 and ±0.010 dB, respectively. A detailed uncertainty analysis can be seen in the discussion in Figure S10. It should be stressed that these uncertainty values are from ΔS_{21} measurements themselves and not from the empirically derived material coefficients. The coefficients α and H_{int} are heavily dependent on the best-fit line location, and any nonideal phenomena occurring throughout the VNA−FMR spectra can cause deviations from the ideal single NP model. Thus, these coefficients should be treated as estimates, as they were calculated for a portion of the VNA−FMR spectra that exhibited linearity.

To summarize the findings in this paper, the parameters for both the 20.2 and 7.3 nm average diameter magnetite NPs can be read in Table 1.

Table 1. Table Summarizing Measured LLG Parameter Results for both the 20.2 nm and 7.3 Average Diameter Magnetite NPs

parameter	20.2 nm	7.3 nm
α	0.32	0.27
H_{int} (Oe)	923.5	416
K_1 (J/m^3)	1/11 K_1	1/80 K_1
M_s (emu/g)	76.3	8.7
f_{res} at H_{DC} of 18.1 Oe (GHz)	2.77	1.96

To eventually apply these results for EO/RF sensors for average power measurements (keeping in mind that one would need a large electric field to have a magnetic field component that can result in the magnetite nanocrystals to thermally heat up), one can start with Rosensweig's equation brought up earlier in this paper. Since RF measurements using thermal changes are average power measurements, it would be best to start Rosensweig's equation with P_{avg}. Since the imaginary component is frequency-dependent, a change can be made to make χ'' into $\chi''(f)$. In addition, the magnetic field H_0 can be updated to H_{AC} to signify that the magnetic field contribution comes from the incident RF field. This modifies the equation to $P_{avg} = \mu_0 \pi \chi''(f) f H_{AC}^2$.[32] As a first-order approximation, one can use the derived first-principles equation of the gyromagnetic precessional response of a magnetite nanocrystal using the following equation: $\chi_{xx}(\omega) = \frac{\gamma M_s[\gamma(H_0 + H_K) - j\alpha\omega]}{(\gamma(H_0 + H_k) - j\alpha\omega)^2 - \omega^2} \frac{1}{4\pi}$,

https://doi.org/10.1021/acsomega.4c04589
ACS Omega 2024, 9, 41433−41445

where H_k (in A/m) is $\frac{2K}{M_s}$, with K being the magnetic anisotropic coefficient in J/m^3 and M_s being the magnetization saturation in emu/g. H_0 (in A/m) is $(H_{DC} + H_{int}) \times 79.577$, where H_{DC} and H_{int} are in Oe (the 79.577 conversion term keeps it in terms of A/m). Finally, ω is the angular frequency of the RF field ($2\pi f$). The reader is encouraged to read the referenced literature for the full derivation.[26] For most accurate results, it is recommended to use a Ubermag, which is a freely accessible FDTD micromagnetics Python code to all readers.[43] One can then take the imaginary contribution of $\chi_{xx}(\omega)$ and insert it into the modified Rosensweig's equation to get the average heating power of the magnetite NPs. By itself, the average power from Rosensweig's is in terms of the material in general, not by the amount of material. Specific absorption rate (SAR) is a useful parameter to then tie the thermal power in terms of the amount of material used. In this case, the SAR is $\mathrm{SAR} = \frac{P_{avg}}{\rho V}$ in units of (W/kg), where V is the volume of an individual nanocrystal and ρ is the density of the material. The density of bulk magnetite is 5.18 g/cm^3.[44] The spherical volume of the 20.2 nm average diameter magnetite NP is 4315.7 nm^3 and that of the 7.3 nm average diameter magnetite NP is 203.7 nm^3. From here, one can then start to engineer an RF sensor by determining the mass of NPs of a given average diameter needed to reach a desired SAR. From here, one can use a well-known partial differential equation called the heat transfer equation: $Q = \rho c\frac{\partial T}{\partial t} - \nabla\cdot(k\nabla)$ where Q would be the thermal energy in joules, ρ is the density of the material, c is the heat capacity, T is the temperature, and k is the coefficient of heat conduction. From here, one can model the thermal transfer of heat from the magnetite nanocrystal to a neighboring QD. At this point, it is up to the engineer to decide whether it would be more effective to use a thermoelectric material to be an RF transducer or use optical materials sensitive to thermal changes. We propose and recommend using optical materials (specifically QDs or NPLs) since if one would be to use magnetite NPs for free-field RF sensing, the strength of the electric field would be large and any electrical materials could potentially be disrupted by such fields. Instead, using optical materials can provide electrical isolation and can be integrated within fiber optics. Additional details regarding how one can integrate nanomaterials through a fiber optic cable called PCFs can be read in the referenced material.[45] In terms of how one can integrate QDs with magnetite NPs, a recommended approach would be to create nanoclusters where QDs outnumber the number of magnetite NPs and are separated only by the length of the ligands (organic surfactants to prevent agglomeration) between the two different NPs. QDs can have their optical photoluminescent emission wavelength shift modeled by the Varshni relation: $E_g(T) = E_g(0) - \alpha\frac{T^2}{T+\beta}$, where α is the temperature coefficient, β is the parameter related to the Debeye temperature of the semiconducting material, and $E_g(0)$ is the energy gap at 0 K.[46,47] Another method could be to measure the PL emission decay time from the QDs which is also sensitive to thermal changes.[48] From here, one can then perform an optical link budget analysis of their EO/RF sensor. The core limitations of the SNR would be with the amount of magnetite and QD material used, the sensitivity of the optical detector, optical coupling losses, the power of the optical excitation source for the QDs, and any amplification systems used. The use of these EO/RF probes can become very important new diagnostic tools in high-powered microwave and high-powered microwave applications. For additional information, please refer to the ref 49.

One additional point needs to be considered: pulsed RF fields could be measured, but there is a practical limit to which magnetite NPs would be sensitive to. The full thermal heating capacity of magnetite NPs under gryomagnetic precessional heating occurs after a RF field irradiates the magnetite NPs for at least 1 ns.[23] This means that pulses with a FWHM of less than 1 ns will be difficult to detect with QDs can detect. However, beyond 1 ns, thermal heat is immediately generated by the magnetite NPs and that heat will travel to nearby QDs. Provided that the QDs can be heated long enough to increase in temperature, measuring the average power of a pulsed measurement is possible. However, it is important to note that the average power can only consider changes in the pulse that occur longer than 1 ns; otherwise, peak powers that appear essentially as delta impulses may not be measured at all. Fortunately, there exists an application space where electric fields in excess of 10 s of kV/m can exist in free-field space and a fwhm longer than a couple of nanoseconds. This could be either in the open air or within a gigahertz transverse electromagnetic (GTEM cell).[49−51]

5. CONCLUSIONS

We have investigated two different average diameters (20.2 and 7.3 nm) of colloidal Fe_3O_4 NPs dried as a film on a microstrip. From VNA−FMR measurements, we can conclude that the larger diameter NPs have a lower MHz/Oe slope than the smaller one. Further analysis was carried out to determine the best way to estimate the material coefficients (α and H_{int}) by using the best-fit line technique. We found that previous papers did not fully explain all the intricacies one must consider when applying the best-fit line methodology to calculate the material coefficients. By investigating two different diameters of magnetite NPs, we established that care must be taken when using the K_1 coefficient for their micromagnetic simulations. The imaginary susceptibility of the micromagnetic simulation does not match the ΔS_{21} spectrum in the linear region without further adjustment of the K_1 coefficient from a mean randomly distributed magnetic anisotropy directions value of $K_1\frac{1}{2}$ (assumption of mean random orientation of the magnetic dipoles—all magnetic dipoles have random orientations, therefore their magnetic anisotropy averages out). Of note, the larger 20.2 nm NPs only needed to be slightly adjusted by $K_1\frac{1}{11}$ compared to $K_1\frac{1}{2}$ instead of the smaller diameter 7.3 nm NPs, which required a large adjustment of $K_1\frac{1}{80}$. This finding indicates that the larger 20.2 nm NP demonstrates close to an ideal mean randomly distributed magnetic anisotropy of magnetite NP material compared to the smaller 7.3 nm NP.

As an important finding for the further study of magnetite NPs using the measurement technique of VNA−FMR, we estimated the necessary amounts of magnetite within the limitations of this VNA−FMR measurement setup that need to be applied across a microstrip in order to produce VNA−FMR spectra. This amount is ≈0.5 μg across a 4.14 μm × 1.7 mm surface area of microstrip. Without using at least this amount, we encounter low SNR of ΔS_{21} measurement and are unable to reliably calculate material coefficients. We also performed an

https://doi.org/10.1021/acsomega.4c04589
ACS Omega 2024, 9, 41433−41445

in-depth analysis of the uncertainties with the VNA−FMR measurements for the applied H_{DC} magnetic field, the VNA itself, and the RF cable connections. A detailed look into the source of error when not subtracting out a control microstrip was presented, and we speculated that using magnetic material within an RF cable (despite using nonmagnetic materials for the microstrip PCB) can have a significant influence on VNA−FMR measurements. In addition, it was important for researchers to disclose the S_{11} of their VNA−FMR setup after loading magnetite NPs due to their influence of the S_{11} and the uncertainty of their setup.

When applying this work for passive sensing applications, we observed the resonant response when no H_{DC} field is applied (at least when making use of their interparticle interactions in the nonlinear regime) trending upward with particle size for the measured SPM magnetite NPs. The 20.2 nm NPs are best used for ≈2.77 GHz RF sensing. This ≈2.77 GHz resonant loss frequency toward a H_{DC} of 0 Oe is projected to increase in frequency with larger diameter NPs. In addition, the magnitude of this resonant loss is projected to increase when referencing the ΔS_{21} spectra between 7.3 and 15 nm[20] and the 20.2 nm magnetite NPs. Since magnetite NPs respond to magnetic fields and not electric fields, they come with an inherent challenge of being able to measure free-space RF fields. Since the wave impedance in air is 377 Ω, an electric field 377 times larger than the magnetic field is required to enable a response for these NPs. However, this high RF electric field requirement could be lessened by embedding the NPs within a dielectric material that changes the wave impedance (the electric field required could then be less than 377 times larger than the magnetic field). Practically speaking, this means that electric fields need to be theoretically at least 10 s of kV/m to allow these magnetite NPs to sense RF by using their thermal changes.[20,23] Another use case can be for near-field RF measurements; however, one must take into consideration the location of the *H*-field. In the case of measuring the RF near-field of microstrip lines, magnetite NPs could be used in measuring the average power RF fields flowing through these lines if given a sufficient amount of RF power (on the order of watts).

■ ASSOCIATED CONTENT

Supporting Information

The Supporting Information is available free of charge at https://pubs.acs.org/doi/10.1021/acsomega.4c04589.

SAXS curves of both 20.2 nm NPs and 7.3 nm NPs materials, absorption spectra, PCB design, CST Studio Suite simulation of microstrip line, RF measurements of control microstrip line, magnetite film application photographs, forward-looking infrared thermal measurements, control ΔS_{21}, changing amount of applied magnetite NPs, uncertainty considerations, zero field cooling, film thickness profile, ferrous material impurity check, magnetite film mass measurement profile, and XRD pattern of magnetite NPs (PDF)

■ AUTHOR INFORMATION

Corresponding Author

Michael D. Sherburne − *Johns Hopkins University Applied Physics Laboratory, Laurel, Maryland 20723, United States;* orcid.org/0000-0002-3851-2058; Email: michael.sherburne@jhuapl.edu

Authors

Timothy A. Dreier − *Sandia National Laboratory, Albuquerque, New Mexico 87185-1421, United States*

Benjamin H. Klitsner − *Sandia National Laboratory, Albuquerque, New Mexico 87185-1421, United States*

Dale L. Huber − *Sandia National Laboratory, Albuquerque, New Mexico 87185-1421, United States;* orcid.org/0000-0001-6872-8469

Sergei A. Ivanov − *Los Alamos National Laboratory, Albuquerque, New Mexico 87123, United States;* orcid.org/0000-0001-6790-5187

Chris Parks − *National Institute of Standards and Technology, Boulder, Colorado 80305-3337, United States*

Matt T. Simons − *National Institute of Standards and Technology, Boulder, Colorado 80305-3337, United States*

Edl Schamiloglu − *Department of Electrical and Computer Engineering, University of New Mexico, Albuquerque, New Mexico 87131-0001, United States*

Complete contact information is available at: https://pubs.acs.org/10.1021/acsomega.4c04589

Notes

The authors declare no competing financial interest.

■ ACKNOWLEDGMENTS

The authors thank N. Erickson, J. McConaha, and H. Sommerdyke for their assistance in the calibration of the VNA. The authors also thank M. Elag, A. Keffer, and R. Frevert for their work on the journal cover art. This work was performed, in part, at the Center for Integrated Nanotechnologies, an Office of Science User Facility operated by the U.S. Department of Energy (DOE) Office of Science. Sandia National Laboratories is a multimission laboratory managed and operated by National Technology Engineering Solutions of Sandia, LLC, a wholly owned subsidiary of Honeywell International, Inc., for the U.S. DOE's National Nuclear Security Administration under contract DE-NA-0003525. The views expressed in this article do not necessarily represent the views of the U.S. DOE or the United States Government. Los Alamos National Laboratory, an affirmative action equal opportunity employer, is managed by Triad National Security, LLC for the U.S. Department of Energy's NNSA, under contract 89233218CNA000001.

■ REFERENCES

(1) Owens, I.; Grabowski, C.; Biller, A.; Ulmen, B.; Joseph, N.; Hughes, B.; Coffey, S.; Kirschner, D.; Struve, K. Electro-optical measurement of intense electric field on a high energy pulsed power accelerator. *Sci. Rep.* **2021**, *11*, 10702.

(2) Staniec, K.; Jóskiewicz, Z.; Janukiewicz, J.; Wieckowski, T. International Journal of Electronics and Telecommunications. *Int. J. Electron. Telecommun.* **2020**, *66*, 107−123.

(3) Maurice, O.; Lafon, F.; de Daran, F.; Oussedrat, R.; Yacoub, I. B. GTEM Cell Facility Use During Project Development Phases for Automotive. In *3rd International Workshop on Electromagnetic Compatibility of Integrated Circuits*, 2002; pp 19−22.

(4) Lumiloop. Sensors in Extreme Areas. Online. 2020, http://lumiloop.de/en/products (accessed October 1, 2022).

(5) Kapteos. KAPTEOS Products Services. Online. 2021, https://en.kapteos.com/products-services (accessed October 1, 2022).

(6) SPEAG. ICEy TDS E-field Probes: E1TDSx, E1TDSz. Online. 2020, https://speag.swiss/products/icey/icey-emc/ (accessed October 1, 2022).

(7) Giken, S. Optical probe for malfunction noise. Online. 2015, https://www.seikoh-giken.co.jp/en/products/mix9.html (accessed October 1, 2022).
(8) Aldena. Selective Electric Probe. Online. 2021, https://www.aldena.it/sep-selective-electric-probe/ (accessed October 1, 2022).
(9) McLean, J. S. A re-examination of the fundamental limits on the radiation Q of electrically small antennas. *IEEE Trans. Antenn. Propag.* **1996**, *44*, 672.
(10) Giri, D. *High-Power Electromagnetic Radiators: Nonlethal Weapons and Other Applications*; Harvard University Press, 2004.
(11) Assimonis, S. D.; Fusco, V.; Georgiadis, A.; Samaras, T. Efficient and Sensitive Electrically Small Rectenna for Ultra-Low Power RF Energy Harvesting. *Sci. Rep.* **2018**, *8*, 15038.
(12) Behague, F.; Calero, V.; Coste, A.; Godet, A.; Suarez, M.; Gaborit, G.; Duvillaret, L.; Baida, F. I.; Bernal, M.-P.; Courjal, N. Minimally invasive optical sensors for microwave-electric-field exposure measurements. *J. Opt. Microsyst.* **2021**, *1*, 020902.
(13) Calero, V.; Suarez, M. A.; Salut, R.; Baida, F.; Caspar, A.; Behague, F.; Courjal, N.; Galtier, L.; Gillette, L.; Duvillaret, L.; Gaborit, G.; Bernal, M. P. An ultra wideband-high spatial resolution-compact electric field sensor based on Lab-on-Fiber technology. *Sci. Rep.* **2019**, *9*, 8058.
(14) Aobaid, R. A.; Hussain, H. S. Magneto-optical sensor based on the bandgap effect of a hollow-core photonic crystal fiber injected with Fe_3O_4. *IOP Conf. Ser.: Mater. Sci. Eng.* **2020**, *871*, 012068.
(15) Miao, Y.; Liu, B.; Zhang, K.; Liu, Y.; Zhang, H. Temperature tunability of photonic crystal fiber filled with Fe_3O_4 nanoparticle fluid. *Appl. Phys. Lett.* **2011**, *98*, 021103.
(16) Taghizadeh, M.; Bozorgzadeh, F.; Ghorbani, M. Designing magnetic field sensor based on tapered photonic crystal fibre assisted by a ferrofluid. *Sci. Rep.* **2021**, *11*, 14325.
(17) Thakur, H. V.; Nalawade, S. M.; Gupta, S.; Kitture, R.; Kale, S. N. Photonic crystal fiber injected with Fe_3O_4 nanofluid for magnetic field detection. *Appl. Phys. Lett.* **2011**, *99*, 161101.
(18) Zu, P.; Chiu Chan, C.; Gong, T.; Jin, Y.; Chang Wong, W.; Dong, X. Magneto-optical fiber sensor based on bandgap effect of photonic crystal fiber infiltrated with magnetic fluid. *Appl. Phys. Lett.* **2012**, *101*, 241118.
(19) Luong, K. Q. T. Spin Dynamics for Radio Frequency Applications, Ph.D. Thesis, University of California, 2022.
(20) Lee, J.-H.; Kim, B.; Kim, Y.; Kim, S.-K. Ultra-high rate of temperature increment from superparamagnetic nanoparticles for highly efficient hyperthermia. *Sci. Rep.* **2021**, *11*, 4969.
(21) Tamaru, S.; Yamamoto, T.; Onuma, T.; Kikuchi, N.; Okamoto, S. Development of a high-sensitivity VNA-FMR spectrometer with field modulation detection and its application to magnetic characterization. *Electron. Commun. Jpn.* **2021**, *104*, No. e12320.
(22) Marks, R.; Williams, D. A general waveguide circuit theory. *J. Res. Natl. Inst. Stand. Technol.* **1992**, *97*, 533.
(23) Lee, J.-H.; Kim, Y.; Kim, S.-K. Highly efficient heat-dissipation power driven by ferromagnetic resonance in MFe_2O_4 (M = Fe, Mn, Ni) ferrite nanoparticles. *Sci. Rep.* **2022**, *12*, 5232.
(24) Psuj, G.; Lopato, P.; Maciusowicz, M.; Herbko, M. A System for Monitoring of Broadband FMR Phenomenon in Low-Carbon Steel Films Subjected to Deformations. *Sensors* **2021**, *21*, 4301.
(25) Kalarickal, S. S.; Krivosik, P.; Wu, M.; Patton, C. E.; Schneider, M. L.; Kabos, P.; Silva, T. J.; Nibarger, J. P. Ferromagnetic resonance linewidth in metallic thin films: Comparison of measurement methods. *J. Appl. Phys.* **2006**, *99*, 093909.
(26) Sherburne, M.; Safonov, V. *Modeling the Ferromagnetic Resonance Response of a Magnetite Nanocrystal Using Both Mathematical First Principles and Ubermag Software*; Defense Technical Information Center, 2022.
(27) Nesbitt, E. A.; Willens, R. H.; Sherwood, R. C.; Buehler, E.; Wernick, J. H. New Permanent Magnet Materials. *Appl. Phys. Lett.* **1968**, *12*, 361−362.
(28) Miyashita, S. *Fundamental Theories of Physics*; Springer Nature Singapore, 2022; pp 175−193.
(29) Victora, R.; Shen, X. Exchange coupled composite media for perpendicular magnetic recording. *IEEE Trans. Magn.* **2005**, *41*, 2828−2833.
(30) Akbarzadeh, A.; Samiei, M.; Davaran, S. Magnetic nanoparticles: preparation, physical properties, and applications in biomedicine. *Nanoscale Res. Lett.* **2012**, *7*, 144.
(31) Li, T. Superparamagnetism. 2020, https://eng.libretexts.org/Bookshelves/Materials_Science/Supplemental_Modules_(Materials_Science)/Magnetic_Properties/Superparamagnetism (accessed October 1, 2022).
(32) Rosensweig, R. Heating magnetic fluid with alternating magnetic field. *J. Magn. Magn. Mater.* **2002**, *252*, 370−374.
(33) Vreeland, E. C.; Watt, J.; Schober, G. B.; Hance, B. G.; Austin, M. J.; Price, A. D.; Fellows, B. D.; Monson, T. C.; Hudak, N. S.; Maldonado-Camargo, L.; Bohorquez, A. C.; Rinaldi, C.; Huber, D. L. Enhanced Nanoparticle Size Control by Extending LaMer's Mechanism. *Chem. Mater.* **2015**, *27*, 6059−6066.
(34) Kittel, C. *Introduction to Solid State Physics*; Wiley: New York, 1976.
(35) Balanis, C. A. *Advanced Engineering Electromagnetics*, 2nd ed.; John Wiley & Sons, 2012; Chapter 4, p 142.
(36) Nuñez, J. R.; Anderton, C. R.; Renslow, R. S. Optimizing colormaps with consideration for color vision deficiency to enable accurate interpretation of scientific data. *PLoS One* **2018**, *13*, No. e0199239.
(37) Gweon, H. K.; Park, H.-J.; Kim, K.-W.; Lee, K.-J.; Lim, S. H. Intrinsic origin of interfacial second-order magnetic anisotropy in ferromagnet/normal metal heterostructures. *NPG Asia Mater.* **2020**, *12*, 23.
(38) Peterson, S. F.; Idzerda, Y. U. Determination of anisotropy constants via fitting of magnetic hysteresis to numerical calculation of Stoner−Wohlfarth model. *AIP Adv.* **2021**, *11*, 085111.
(39) Moreno, R.; Poyser, S.; Meilak, D.; Meo, A.; Jenkins, S.; Lazarov, V. K.; Vallejo-Fernandez, G.; Majetich, S.; Evans, R. F. L. The role of faceting and elongation on the magnetic anisotropy of magnetite Fe_3O_4 nanocrystals. *Sci. Rep.* **2020**, *10*, 2722.
(40) Mørup, S.; Hansen, M. F.; Frandsen, C. Magnetic interactions between nanoparticles. *Beilstein J. Nanotechnol.* **2010**, *1*, 182−190.
(41) Dormann, J.; Fiorani, D.; Cherkaoui, R.; Tronc, E.; Lucari, F.; D'Orazio, F.; Spinu, L.; Noguès, M.; Kachkachi, H.; Jolivet, J. From pure superparamagnetism to glass collective state in γ-Fe_2O_3 nanoparticle assemblies. *J. Magn. Magn. Mater.* **1999**, *203*, 23−27.
(42) Mamiya, H.; Nakatani, I.; Furubayashi, T. Blocking and Freezing of Magnetic Moments for Iron Nitride Fine Particle Systems. *Phys. Rev. Lett.* **1998**, *80*, 177−180.
(43) Beg, M.; Lang, M.; Fangohr, H. Ubermag: Toward More Effective Micromagnetic Workflows. *IEEE Trans. Magn.* **2022**, *58*, 1−5.
(44) Blaney, L. *Magnetite (Fe3O4): Properties, Synthesis, and Applications*, Lehigh Review; Lehigh University, 2007; Vol. *15*.
(45) Sherburne, M.; Harjes, C.; Klitsner, B.; Gigax, J.; Ivanov, S.; Schamiloglu, E.; Lehr, J. Rapid Prototyping for Nanoparticle-Based Photonic Crystal Fiber Sensors. *Sensors* **2024**, *24*, 3707.
(46) Lu, L.; Chen, D.; Zhao, G.; Ren, X.; Guo, G. Temperature and Excitation Wavelength Dependence of Surface-Plasmon-Mediated Emission from CdSe Nanocrystals. *J. Phys. Chem. C* **2010**, *114*, 18435−18438.
(47) Narayanaswamy, A.; Feiner, L. F.; van der Zaag, P. J. Temperature Dependence of the Photoluminescence of InP/ZnS Quantum Dots. *J. Phys. Chem. C* **2008**, *112*, 6775−6780.
(48) Labeau, O.; Tamarat, P.; Lounis, B. Temperature Dependence of the Luminescence Lifetime of Single CdSe/ZnS Dots. *Phys. Rev. Lett.* **2003**, *90*, 257404.
(49) Benford, J.; Swegle, J. A.; Schamiloglu, E. *High Power Microwaves*, 3rd ed.; CRC Press, 2015.
(50) Sherburne, M. D.; Sommerdyke, H. L.; Erickson, N. G.; Harjes, C. D.; McConaha, J. W.; Pohle, H. H. Electric Field Sensor Approach to Determine Fidelity and Overmoding Region of GTEM Cell. *IEEE Sensor. J.* **2023**, *23*, 3640−3646.

https://doi.org/10.1021/acsomega.4c04589
ACS Omega 2024, 9, 41433−41445

(51) Sherburne, M. D.; Harjes, C. D.; Pohle, H. H.; Lehr, J. M. Calibrating a Radio Frequency Electrooptic Sensor for Field-Relevant Temperature Conditions in a Laboratory Setting. *IEEE Sensor. J.* **2023**, *23*, 5849−5857.

https://doi.org/10.1021/acsomega.4c04589
ACS Omega 2024, 9, 41433−41445